https://doi.org/10.5194/tc-2021-329
Preprint. Discussion started: 25 October 2021

The Cryosphere Discussions

Long term analysis of cryoseismic events and associated ground thermal stress in Adventdalen, Svalbard

Rowan Romeyn[1], Alfred Hanssen[1], Andreas Köhler[1,2]

[1]Department of Geosciences, University of Tromsø – The Arctic University of Norway, 9037 Tromsø, Norway
[2]NORSAR, Gunnar Randers vei 15, 2007 Kjeller, Norway

Correspondence to: Rowan Romeyn (rowan.romeyn@uit.no)

Abstract. The small-aperture Spitsbergen seismic array (SPITS) has been in continuous operation at Janssonhaugen for decades. The high Artic location in the Svalbard archipelago makes SPITS an ideal laboratory for the study of cryoseisms, a nontectonic class of seismic events caused by freeze processes in ice, ice-soil and ice-rock materials. We extracted a catalogue of >100 000 events from the nearly continuous observation period between 2004 and 2021, characterized by short duration ground shaking of just a few seconds. This catalogue contains two main subclasses where one subclass is related to underground coal mining activities and the other is inferred to be dominated by frost quakes resulting from thermal contraction cracking of ice wedges or other segregated ice bodies. This inference is supported by the correspondence between peaks in observed seismicity with peaks in modelled ground thermal stress, based on a Maxwellian thermo-viscoelastic model constrained by borehole observations of ground temperature. The inferred frost quakes appear to be dominated by surface wave energy and SPITS proximal source positions, with three main areas that are associated with dynamic geomorphological features; boulder producing scarps and solifluction lobes. Seismic stations providing year-round, high temporal resolution measurements of ground motion may be highly complementary to satellite remote sensing methods, such as InSAR, for studying the dynamics of periglacial environments. The long-term observational record presented in this study, containing tens of thousands of cryoseismic events, in combination with a detailed record of borehole ground temperature observations, provides a unique insight into the spatiotemporal patterns of cryoseisms. The observed patterns may guide the development of models that can be used to understand future changes to cryoseismicity based on projected temperatures.

1 Introduction

Cryoseisms are a nontectonic class of seismic events caused by freeze processes in ice, ice-soil and ice-rock materials (Lacroix, 1980). For example, the buildup of thermal stress in frozen soils during intense periods of cooling can lead to tensional fracturing and explosive pressure release (Barosh, 2000; Battaglia et al., 2016). Since this pressure release triggers the propagation of seismic waves, these events are sometimes referred to as frost quakes (e.g. Okkonen et al., 2020). Observations of frost quakes are limited because seismic amplitudes decay rapidly with distance from the point of rupture, but they have been felt at distances of several hundred meters to several kilometers and are usually accompanied by cracking or booming

https://doi.org/10.5194/tc-2021-329
Preprint. Discussion started: 25 October 2021

noises, resembling falling trees, gunshots or underground thunder (Leung et al., 2017; Nikonov, 2010). Cracking typically occurs in response to rapid air and ground cooling, in the absence of an insulating snow layer and where sufficient moisture is present for ice to form (Barosh, 2000; Battaglia et al., 2016; Matsuoka et al., 2018; Nikonov, 2010). The resulting fractures may potentially cause damage to buildings and other infrastructure in cold regions (Okkonen et al., 2020). Frost heave (e.g. Rempel, 2010) can be understood as a combination of slow creep and rapid elastic (frost quakes) deformation of frozen ground and causes damage to roads requiring billions of dollars annually to repair in the United States alone (DiMillio, 1999).

Ice-wedge or sand-wedge polygons are a widespread manifestation of a dynamic cryosphere observed in the periglacial environment (e.g. Black, 1976; Matsuoka et al., 2004). These structures form when water infiltration and thermal contraction, or wind transported sand grains, hold open fractures which become planes of weakness (Lachenbruch, 1962; Mackay, 1984; Matsuoka et al., 2004; Sørbel and Tolgensbakk, 2002). Repeated cracking, infilling and refreezing along these planes causes the ice wedges to grow laterally, forcing the displaced ground upwards and resulting in a series of ridges in a polygonal arrangement that are one of the most recognizable landforms in permafrost environments (Christiansen et al., 2016; Lachenbruch, 1962; Matsuoka et al., 2018). For this reason, sand-wedge polygons, that were formed at sea level on the paleo-equator during late Neoproterozoic glacial episodes, have been used as evidence supporting the snowball Earth hypothesis (Maloof et al., 2002). Small-scale polygonal features observed on the surface of Mars have also been inferred to result from thermal contraction cracking (Mellon, 1997).

Frost cracking driven by segregation ice growth is also an important agent of bedrock erosion in cold mountainous areas, where active screes and high headwall erosion rates are observed in areas where frost erosion is most intense (Hales and Roering, 2009; Hales and Roering, 2007; Scherler, 2014). Rockfall driven by frost cracking may be the primary mechanism in cold and dry mountain climates (Hales and Roering, 2009). Progressive crack growth is driven by the migration of water to ice bodies in cracks that is similar to the mechanism by which ice lenses develop in freezing soil (Hallet et al., 1991; Murton et al., 2006; Peppin and Style, 2013; Walder and Hallet, 1985). Frost cracking and creep on slopes leads to the development of solifluction lobes and sheets (Cable et al., 2018; Matsuoka, 2001). Solifluction is broadly defined as the slow mass wasting resulting from freeze-thaw action in fine-textured soils (French, 2017; Matsuoka, 2001) and occurs due to the asymmetry between the heaving forces, which are perpendicular with the ground surface and subsequent vertical subsidence under the force of gravity.

Interferometric synthetic aperture radar (InSAR) is a satellite remote sensing technique capable of resolving down to millimeter scale ground surface displacements at a spatial scale of tens of meters (Hanssen, 2001; Rosen et al., 2000). Consequently, InSAR has used to resolve seasonal patterns of frost heave and thaw subsidence (Chen et al., 2020; Rouyet et al., 2021; Wahr et al., 2008). The broad spatial coverage and high spatial resolution of InSAR has also been used to show that the spatial patterns of ground displacement are related to specific geomorphological units, consisting of specific frost prone sediment types and periglacial landforms (Liu et al., 2018; Rouyet et al., 2019). On the other hand, the temporal resolution is determined

https://doi.org/10.5194/tc-2021-329
Preprint. Discussion started: 25 October 2021

by the repeat cycle of the satellite (~6 days for Sentinel-1), which means that it is not possible to distinguish between slow frost creep and rapid elastic deformation (frost quake) processes. In addition, snow cover causes a loss of radar coherence between repeat satellite passes that limits InSAR to snow free areas and times of year. As a result, InSAR is more suited to studying thaw subsidence than frost heave in areas such as Svalbard that are snow covered for the majority of the freezing season (e.g. Rouyet et al., 2019). Seismic stations providing year-round, high temporal resolution measurements of ground motion, at the expense of more limited spatial source resolution and coverage, may be highly complementary to InSAR methods for studying the dynamics of periglacial environments.

This study was motivated by the sporadic observation of clusters of events recorded by the small-aperture Spitsbergen seismic array (SPITS), with durations of just a few seconds and peak amplitudes significantly above the background noise level. For comparison, regional tectonic earthquakes are typically associated with >30 s shaking duration. SPITS has previously been used to study a class of cryoseismic signals associated with iceberg calving at the termini of grounded tidewater glaciers at local to near-regional distances of up to 200 km (Köhler et al., 2015). These calving related seismic signals occurred most frequently during the melt season and the ground motion lasts ~15-20 s. Signals with intermediate durations have also been observed at SPITS, originating from nearby mountain glaciers (Albaric et al., 2021) and coal mining operations (Gibbons and Ringdal, 2006). Based on previous work further down-valley in Adventdalen, e.g. Matsuoka et al. (2018) and Romeyn et al. (2021), we hypothesized that the short duration events at SPITS might be dominated by frost quakes initiated by thermal contraction cracking in the vicinity of the array. The aim of this study was to test this hypothesis by analyzing the spatial and temporal occurrence of these events. This study is highly complementary to the previous work of Romeyn et al. (2021). While the spatial and temporal wavefield sampling of the SPITS array is much coarser than the temporary array they deployed, a much longer and nearly continuous record is available. This allows a more rigorous investigation of the temporal correlation of these events with ground cooling and thermal stress accumulation.

2 Study area and data

The small-aperture Spitsbergen seismic array (SPITS) is located on Janssonhaugen, in the Adventdalen valley on the island of Spitsbergen, part of the Svalbard archipelago (Figure 1). The SPITS array has been in operation since 1992, maintained by the research foundation NORSAR. At present, it consists of 9 CMG-3T seismometers with an aperture of 1 km and interstation distances >250 m (e.g. Gibbons et al., 2011; Köhler et al., 2015) installed in shallow boreholes below the permafrost active layer. The standard frequency response of the CMG-3T seismometer is flat (within -3dB) for the range from 0.0083 to 50 Hz. We chose to limit the present study to the period following August 2004 when the SPITS array was upgraded to a full broadband array with an increase in sampling rate from 40 to 80 Hz for all seismometers (Schweitzer et al., 2021). The waveform data following the upgrade is of high quality and well suited to source localization using broadband, coherent

https://doi.org/10.5194/tc-2021-329
Preprint. Discussion started: 25 October 2021

The Cryosphere Discussions
Open Access
EGU

matched field processing. Waveform data for the SPITS array were retrieved from the European Integrated Data Archive (EIDA), maintained by the University of Bergen and NORSAR.

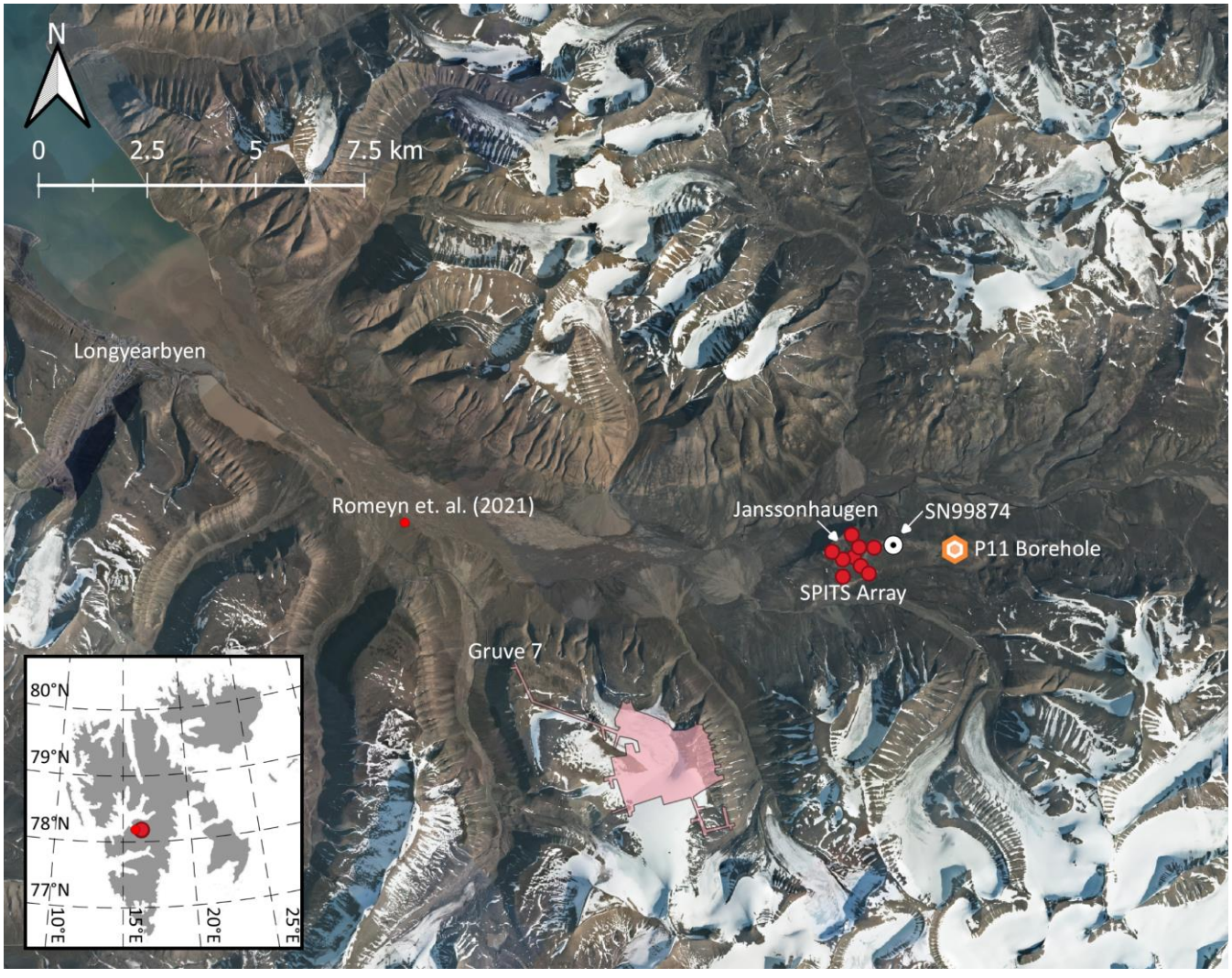

Figure 1 – Overview of the location of the SPITS array located on Janssonhaugen in Adventdalen, up-valley from the settlement of Longyearbyen and the temporary seismic array of Romeyn et al. (2021). The P11 temperature logging borehole and the underground mining areas and tunnels of the operational coal mine, Gruve 7, are also shown. The met.no weather station "Janssonhaugen Vest" is marked by its station number, SN99874. Orthophoto © Norwegian Polar Institute (npolar.no).

Janssonhaugen is a bedrock remnant located in the middle of the Adventdalen valley, with a ~0.2-0.3 m thick weathered sediment crust overlying homogeneous sand-/siltstone bedrock (density 2280kg.m^{-3}, porosity 20-25 %, >96.5 % SiO_2) corresponding to the Ullaberget Member of Lower Cretaceous Rurikfjellet Formation (Dypvik et al., 1991; Isaksen et al., 2001). The bedrock at Janssonhaugen has been drilled to a depth of 102 m and the permafrost zone is estimated to extend down

https://doi.org/10.5194/tc-2021-329
Preprint. Discussion started: 25 October 2021

to 220 m, based on downward extrapolation of the measured temperature gradient (Isaksen et al., 2001). Despite annual precipitation of 300-500 mm/yr., the snow cover on Janssonhaugen is typically thin or completely absent due to the scouring
110 effect of the prevailing winds (Isaksen et al., 2001). The surface topography is generally flat but loose surface material is sorted into polygons (Isaksen et al., 2001), indicating the presence of sand/ice-wedges. The homogeneous geology at Janssonhaugen, it's flat topography, limited snow cover, relatively large distance to glaciers, rivers, ocean, human activity such as coal mining and position well above the Holocene marine limit make it a good location to study permafrost processes (Isaksen et al., 2000).

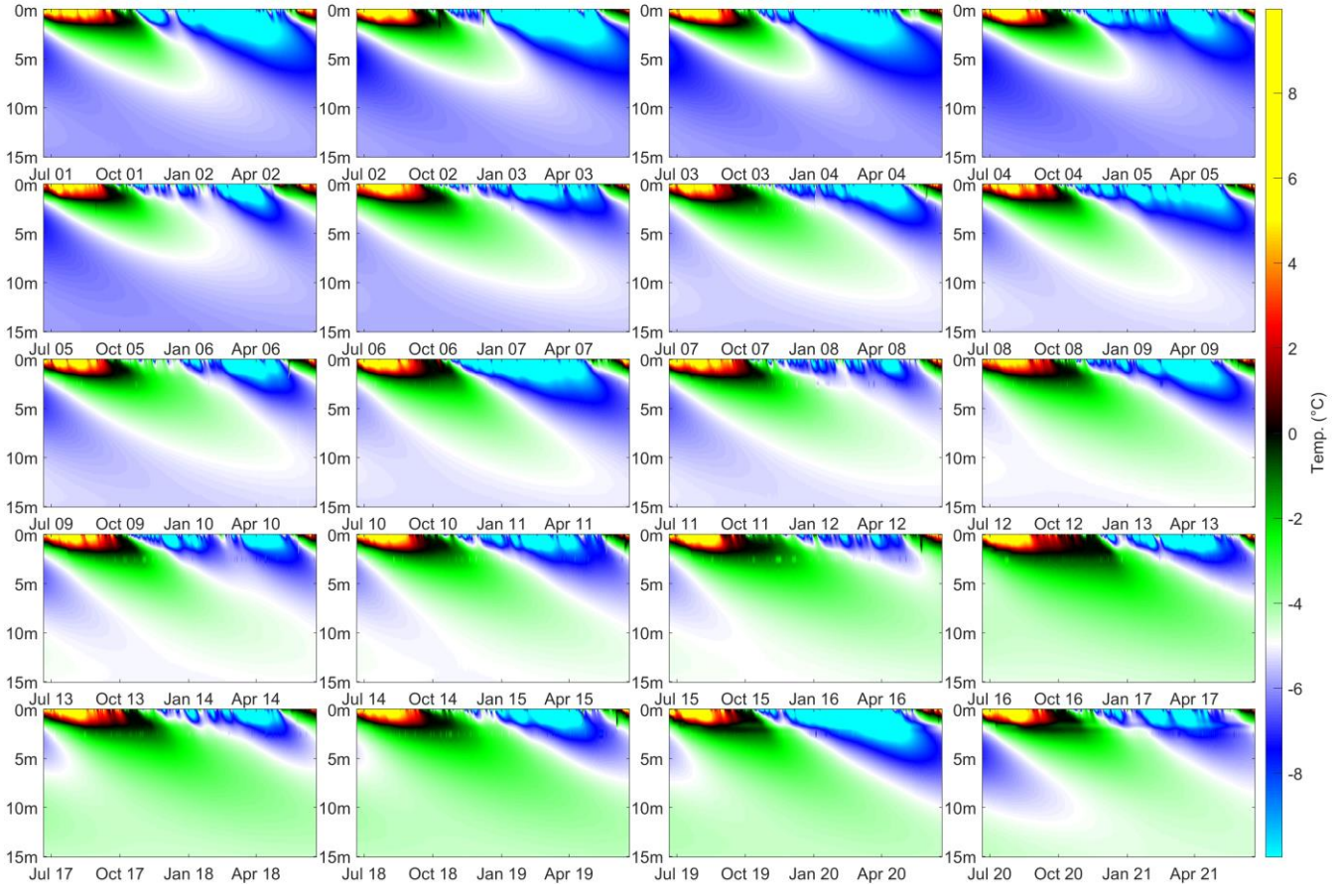

115 **Figure 2 – Illustration of borehole temperature history recorded at the PACE P11 borehole on Janssonhaugen. A long-term warming trend is observed below the active layer that is subject to seasonal freeze-thaw.**

Temperature monitoring boreholes installed at Janssonhaugen are critical to our ability to accurately model the subsurface buildup of thermal stress. Thermistors installed in the GTN-P (Global Terrestrial Network for Permafrost) boreholes P10 (102
120 m deep) and P11 (15 m deep) provide a continuous record of the subsurface temperature field at Janssonhaugen, with a sampling interval of 6 hours extending from April 1999 to the present (Isaksen et al., 2001). We focus on the P11 borehole (see Figure 1), which gives the most detailed record of the near-surface temperature field and is least disturbed by installations

https://doi.org/10.5194/tc-2021-329
Preprint. Discussion started: 25 October 2021

at the ground surface. The temperature field measured by the P11 borehole is illustrated in Figure 2. The ~2 m thick active layer (Christiansen et al., 2020) is sampled by thermistors at 0.2, 0.4, 0.8, 1.2, 1.6 and 2 m and there is significant inter-annual variability in the magnitude of summer warming and winter cooling. A long-term warming trend is observed in the permafrost beneath the active layer (Figure 2). Furthermore, the Janssonhaugen Vest weather station (see Figure 1), which was installed in September 2019, provides an hourly sampled record of ground temperature at 0.1 m depth and provides a basis to compare depth and temporal sampling effects against the longer duration P11 record.

3 Methods

3.1 STA/LTA detection of short duration seismic events

The purpose of the event detector is to make a first-pass automatic identification of short duration seismic signals, which should be distinguished from both background noise and longer duration local and regional seismic events that may be high amplitude. The raw data from each seismometer was first de-trended, corrected according to the calibrated instrument sensitivity and bandpass filtered to the range 2.5-20 Hz using a delay-compensated minimum phase filter with a stopband attenuation of 60 dB (see Figure 3a).

Events are detected based on anomalous values of short-time-averaged amplitude divided by long-time-averaged amplitude, i.e., the classic STA/LTA approach (e.g. Trnkoczy, 2009). In our implementation, the short-term average (STA) from the trace envelope for each seismogram, given by the magnitude of the Hilbert transform and smoothed by taking the one-second moving average. Since we have an array of stations, we represent the array-STA by taking the 80^{th} percentile station-STA across all stations at a given time. By visual inspection of test periods, we found that this emphasizes very local events with large amplitude variation across the array, while still ensuring that there is at least some coherency across the array. If we had chosen the maximum array STA, we may detect arbitrary noise spikes with large amplitudes registered on a single seismometer. If the mean or median array STA were chosen, we would preferentially detect larger regional events with more consistent amplitudes across the array and suppress smaller local events with high amplitudes limited to a small subset of seismometers.

We calculate the long-term average (LTA) by simply smoothing the short-time average according to its moving average over a time-span of 20 seconds. This time-span is significantly longer than the events we seek to detect but shorter than the typical duration of the more regional scale seismic events that we want to ignore. We further reject epochs with LTA more than 2.5x the 2-hourly mean LTA in order to filter out large regional events. Events are then detected by applying a peak finding routine to the STA/LTA ratio. The STA/LTA peaks must have amplitude ≥10 and occur at least 5 seconds apart from one another. An example of event detection based on STA/LTA peaks is shown in Figure 3b, which illustrates that short duration events are selected while a longer high-amplitude event is not detected as intended.

https://doi.org/10.5194/tc-2021-329
Preprint. Discussion started: 25 October 2021

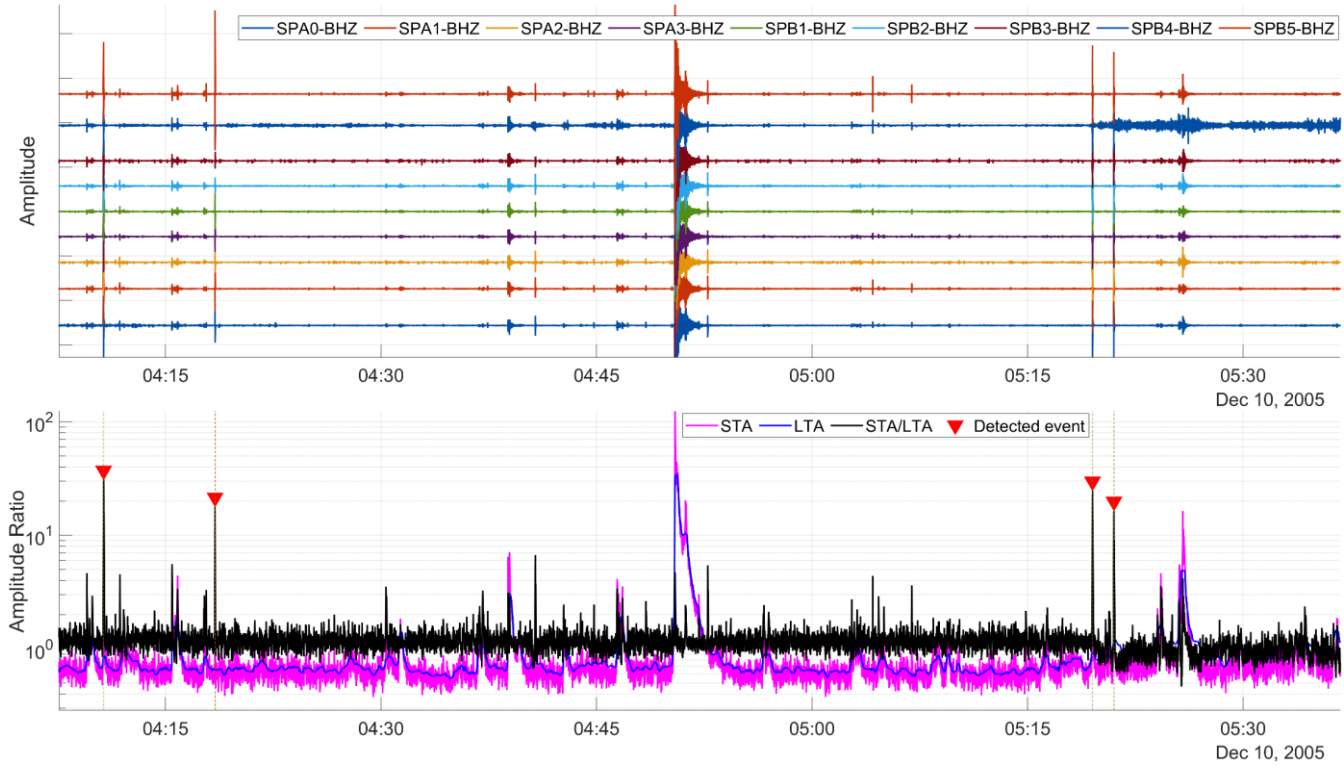

Figure 3 – Example of event detection using the STA/LTA (short term/long term average) detector. Short duration events with sufficient amplitude and array coherence are selected while longer events such as the high amplitude example at 04:50 are ignored.

3.2 Source localization by coherent MFP

Matched-field processing (MFP) is an established technique for localizing the position of seismic sources recorded by passive seismic arrays (Chmiel et al., 2016; Cros et al., 2011; Harley and Moura, 2014; Sergeant et al., 2020; Walter et al., 2015). MFP proceeds via an evaluation of the similarity between the wavefield recorded at a receiver array and a series of predicted wavefields calculated for a grid of test source locations and a theoretical model of the source-receiver wave propagation. The MFP coherence is estimated by comparing the recorded data vector with a "replica" vector, which is a model representation of wave propagation within the medium. We assume a simple homogeneous medium with amplitude decay according to spherical divergence where the replica column vector, $\boldsymbol{R}'$ is represented by the theoretical harmonic wave emitted from a test point $p(x, y)$ according to

$$\boldsymbol{R}'(\omega, \boldsymbol{d}) = \left[\frac{1}{d_1} e^{i\omega d_1/c(\omega)}, \frac{1}{d_2} e^{i\omega d_2/c(\omega)}, \ldots, \frac{1}{d_N} e^{i\omega d_N/c(\omega)}\right]^T /\eta. \quad (1)$$

Here, $i = \sqrt{-1}$, ω is the angular frequency, $\boldsymbol{d} = [d_1, d_2, \cdots, d_N]^T$ is an $N \times 1$ vector containing the absolute Euclidean distances between $p(x, y)$ and the N recording stations where superscript T denotes a transpose, $c(\omega)$ is the medium phase

https://doi.org/10.5194/tc-2021-329
Preprint. Discussion started: 25 October 2021


The Cryosphere Discussions
Open Access
EGU

velocity at frequency ω and the vector is normalised to unit length by dividing by the factor $\eta = \sqrt{\sum_{j=1}^{N}(1/d_j^2)}$. The column

170 data vector is given by

$$\boldsymbol{R}(\omega) = [R_1(\omega), R_2(\omega), \dots, R_N(\omega)]^T, \quad (2)$$

where $R_j(\omega)$ is a frequency transform of the j-th trace $r_j(t)$ of N traces recording a specific seismic event. We then form the complex-valued $N \times N$ cross-spectral density matrix (CSDM) by

$$\mathbf{K}(\omega) = \boldsymbol{R}(\omega)\boldsymbol{R}^H(\omega), \quad (3)$$

175 where $(\cdot)^H$ denotes the Hermitian (conjugate transpose) operator. The frequency domain transform was implemented via the chirp z-transform (Rabiner et al., 1969), which provides a convenient means to evaluate the band limited transform (we select the 5-35 Hz band) with a specific frequency sampling interval (1 Hz). This allows us to efficiently and compactly represent the CSDM, whose size is a significant factor in the speed of computation, in addition to the number of test source points, $p(x, y)$. Conventionally, the MFP coherence is estimated using the linear Bartlett processor

180 $$G = \sum_{\omega} \boldsymbol{R}'^H(\omega, \boldsymbol{d})\mathbf{K}(\omega)\boldsymbol{R}'(\omega, \boldsymbol{d}) \quad (4)$$

which evaluates the inner product between the recorded and predicted wavefields before summing incoherently across frequency.

In this study we implement the coherent MFP scheme developed by Michalopoulou (1998), which is an elegant addition to the

185 conventional approach allowing cross-frequency spatial coherence structures to be exploited to give improved robustness and accuracy. In this scheme, measurement vectors at L discrete frequencies are concatenated to form the $NL \times 1$ measurement super-vector

$$\boldsymbol{\mathcal{R}}(\boldsymbol{\omega}) = [\boldsymbol{R}(\boldsymbol{\omega_1}), \boldsymbol{R}(\boldsymbol{\omega_2}), \cdots, \boldsymbol{R}(\boldsymbol{\omega_L})]^T, \quad (5)$$

where $\boldsymbol{\omega} = [\omega_1, \omega_2, \cdots, \omega_L]^T$ is a frequency vector, and the replica vectors are concatenated to form the $NL \times 1$ replica super-

190 vector

$$\boldsymbol{\mathcal{R}}'(\boldsymbol{\omega}, \boldsymbol{d}) = [\boldsymbol{\mathcal{R}}'(\boldsymbol{\omega_1}, \boldsymbol{d}), \boldsymbol{\mathcal{R}}'(\boldsymbol{\omega_2}, \boldsymbol{d}), \cdots, \boldsymbol{\mathcal{R}}'(\boldsymbol{\omega_L}, \boldsymbol{d})]^T. \quad (6)$$

The super-CSDM $\boldsymbol{\mathcal{K}}(\boldsymbol{\omega}) = \boldsymbol{\mathcal{R}}(\boldsymbol{\omega})\boldsymbol{\mathcal{R}}^H(\boldsymbol{\omega})$ is then composed of $NL \times NL$ elements and the generalized MFP coherence is given by

$$\mathcal{G} = \boldsymbol{\mathcal{R}}'^H(\boldsymbol{\omega}, \boldsymbol{d})\, \boldsymbol{\mathcal{K}}(\boldsymbol{\omega})\, \boldsymbol{\mathcal{R}}'(\boldsymbol{\omega}, \boldsymbol{d}). \quad (7)$$

195 The estimated source position, $p(x, y)$, and phase velocity, $c(\omega)$, are those which maximize the coherence measure $\mathcal{G}$. Since some of the seismic events we wish to locate are dominated by surface waves and others are dominated by body waves, we simply assume that phase velocity is a constant and scan over the range 250-6000 m/s.

https://doi.org/10.5194/tc-2021-329
Preprint. Discussion started: 25 October 2021


The Cryosphere Discussions

3.3 Ground thermal stress model

Previous studies such as Mellon (1997), Maloof et al. (2002), Schulson and Duval (2009) and Podolskiy et al. (2019) have demonstrated that ice and frozen soil deform elastically on short timescales and viscously on long timescales. Thermal loading due to temperature changes acts as an external driving agent, and the resulting dynamical balance between the elastic and viscous response governs whether creep or fracture become dominant. Following Mellon (1997), we model the frozen soil as a Maxwellian viscoelastic solid augmented with thermal expansion and contraction. This allows us to decompose the total strain tensor ε_{ij} into three components: an elastic (ε_{ij}^{e}), a thermal (ε_{ij}^{T}), and a viscous (ε_{ij}^{V}) component,

$$\varepsilon_{ij} = \varepsilon_{ij}^{e} + \varepsilon_{ij}^{T} + \varepsilon_{ij}^{V}, \tag{8}$$

where subscripts ij indicate tensor components, $i, j = 1,2,3$, where 1 and 2 denote horizontal components, and 3 is the vertical component. The elastic strain tensor is related to the stress tensor σ_{ij} by (e.g., Landau and Lifshitz, 1970)

$$\varepsilon_{ij}^{e} = \frac{1+\nu}{E}\,\sigma_{ij} - \frac{\nu}{E}\,\sigma_{kk}\,\delta_{ij}\,, \tag{9}$$

where ν is Poisson's ratio, E is Young's modulus, δ_{ij} is the Kronecker delta, and Einstein's summation convention is applied throughout this paper.

The thermal strain tensor is a measure of the change in volume caused by the thermally driven deformation, and it is expressed as (e.g., Landau and Lifshitz, 1970)

$$\varepsilon_{ij}^{T} = \alpha(T - T_0)\,\delta_{ij}\,, \tag{10}$$

where T is the temperature, T_0 is a reference temperature for the undeformed state, and α is the linear thermal expansion coefficient. The viscous strain tensor is a complicated topic in itself, and a wide range of phenomenological and heuristic parametric models for the viscous strain rate exist (e.g. Bingham, 1922; Carreau, 1972; Glen, 1955; Herschel, 1926; Saramito, 2007). To encompass this generality, we formulate the viscous strain rate as

$$\frac{\partial \varepsilon_{ij}^{V}}{\partial t} = \Gamma_N\{s_{ij}\}, \tag{11}$$

where $\Gamma_N\{\cdot\}$ is a nonlinear operator acting on the deviatoric stress $s_{ij} = \sigma_{ij} - \sigma_{kk}/3$. The chosen parametric form of $\Gamma_N\{\cdot\}$ determines how induced stress relaxes in the medium, and both Newtonian and non-Newtonian behavior can be incorporated in this formulation.

Following Mellon (1997), we assume $\sigma = \sigma_{11} = \sigma_{22}$ and $\partial\varepsilon_{11}/\partial t = \partial\varepsilon_{22}/\partial t = 0$. We assume that Poisson's ratio, $\nu = \nu(T)$, Young's modulus, $E = E(T)$, and the coefficient of linear thermal expansion, $\alpha = \alpha(T)$ are all temperature dependent, and thus, implicitly time dependent since $T = T(z,t)$ is the temperature at depth z and time t. By direct evaluation of $\partial\varepsilon_{ij}/\partial t$ and collecting terms, we find that the temporal dynamics of horizontal stress $\sigma(z,t)$ in a Maxwellian viscoelastic solid driven

https://doi.org/10.5194/tc-2021-329
Preprint. Discussion started: 25 October 2021


The Cryosphere Discussions

by thermal expansion and contraction is governed by the following first-order nonlinear and nonhomogeneous differential equation

$$\frac{\partial \sigma}{\partial t} + \beta(t)\sigma + \Gamma\{\sigma\} = \kappa(t). \quad (12)$$

The time-dependent coefficients are found to be

$$\beta(t) = -\left(\frac{1}{E}\frac{\partial E}{\partial T} + \frac{1}{1-\nu}\frac{\partial \nu}{\partial T}\right)\frac{\partial T}{\partial t}, \quad (13)$$

$$\kappa(t) = -\frac{E}{1-\nu}\left[\alpha + \frac{\partial \alpha}{\partial T}(T - T_0)\right]\frac{\partial T}{\partial t}, \quad (14)$$

and $\Gamma\{\cdot\} = \frac{E}{1-\nu}\,\Gamma_N\{\cdot\}$. The scientific literature devoted to the rheology of frozen materials favor power-law parametrizations for the viscous term (e.g., Schulson and Duval, 2009). In this paper, we apply the heuristic temperature dependent power-law proposed by Glen (1955) in the form used by Mellon (1997) and Maloof et al. (2002):

$$\Gamma\{\sigma\} = \frac{E}{1-\nu} A_0 \left|\frac{\sigma}{2}\right|^n \mathrm{sign}(\sigma)\exp(-Q/RT). \quad (15)$$

In Glen's flow law, R is the universal gas constant, and A_0, Q, and n are empirical parameters that need to be chosen. The temperature-dependent Arrhenius exponential term in this particular choice of $\Gamma\{\cdot\}$ is included to model the increasing ductility as the temperature increases (e.g. Glen, 1955). To sum up, the first two terms on the left-hand side in Eq. (12) are connected to the elastic response of the solid, the third term models viscous relaxation, and the right-hand side is the thermal driving term. In order to solve Eq. (12) for $\sigma(z,t)$, we specify the initial condition $\sigma_0(z) = \sigma(z, t = 0) = 0$.

If we assume $\partial\nu/\partial T = 0$, Eq. (12) reduces to the model proposed by Mellon (1997). By contrast, if we assume $\partial\nu/\partial T = \partial E/\partial T = \partial\alpha/\partial T = 0$, Eq. (12) reduces to the model proposed by Podolskiy et al. (2019). Finally, if we assume $\partial\nu/\partial T = \partial E/\partial T = \partial\alpha/\partial T = A_0 = 0$, Eq. (12) reduces to the Timoshenko and Goodier (1951) model for thermal stress as applied by Okkonen et al. (2020), excluding the boundary correction terms that represent compressive stresses at the free surfaces of the finite thickness plate assumed by the latter authors.

We solved Eq. (12) numerically using the standard Matlab solver ode45, based on the well-known fifth-order Runge-Kutta method (Dormand and Prince, 1980). Notably, most previous studies of subsurface thermal stress have relied on thermal conduction models in order to infer subsurface temperature variation from measurements of air temperature. A significant novelty of this study is that the ground temperature profile, $T(z,t)$, at Janssonhaugen has been logged by a series of thermistors installed in the 15 m deep P11 borehole at 6 hr intervals since April 1999. We assume the stress at a given depth is decoupled from the stress at adjacent depths (Mellon, 1997) and solve Eq. (12) for the temperature timeseries at the selected depth of investigation. The set of physical parameters that we assume is described in Table 1.

https://doi.org/10.5194/tc-2021-329
Preprint. Discussion started: 25 October 2021

Table 1 - Physical parameters used in thermal stress model

Parameter	Symbol, Unit	Value or Equation	Note or reference
T at zero stress state	$T_0, °C$	0	Initial reference temperature
Poisson's ratio	$\nu, -$	$\begin{cases} 0.3 & T \geq 0 \\ 0.008T + 0.3 & -10 \leq T < 0 \\ 0.00067T + 0.23 & T < -10 \end{cases}$	Generalized from Hu et al. (2013) alluvium, Istomin and Nazarov (2019) and Zhankui et al. (1998)
Young's modulus	E, GPa	$\begin{cases} 0.7 & T \geq 0 \\ -0.73T + 0.7 & -10 \leq T < 0 \\ -0.047T + 7.5 & T < -10 \end{cases}$	Generalized from Draebing and Krautblatter (2012); Timur (1968); Weeks and Assur (1967); Wu et al. (2017) small-strain dynamic elastic modulus of ice, permafrost and frozen rock measured by seismic waves
Linear thermal expansion coefficient	$\alpha, °C^{-1}$	$\begin{cases} 10^{-6}\begin{pmatrix} -0.000237T^3 \\ +0.00885T^2 \\ -0.1852T + 52.52 \end{pmatrix} & T \leq 0 \\ 10^{-6}\begin{pmatrix} -0.0621T^2 \\ +5.78T - 22.3 \end{pmatrix} & T > 0 \end{cases}$	Butkovich (1959) gives 3rd order polynomial for ice and a 2nd order polynomial was fitted to Kell (1967) water thermal expansion data
Viscous pre-factor	$A_0, s^{-1}Pa^{-n}$	1×10^{-9}	Glen's non-Newtonian power law viscous flow (Behn et al., 2021; Glen, 1955; Weertman, 1983)
Viscous activation energy	$Q, J\ mol^{-1}$	1.34×10^5	
Viscous exponent	$n, -$	3.2	
Gas constant	$R, J\ mol^{-1}K^{-1}$	8.314	T converted to Kelvin when evaluating RT
Tensile strength	σ_T, MPa	1.0 (range from 0.8-1.3 given in reference)	Currier and Schulson (1982), varies according to grain size for randomly oriented polycrystalline ice (finer grained ice stronger).

3.3.1 Fracture model

We apply a simplistic model of fracturing by considering the modelled thermal stress as the potential stress. When the potential stress exceeds the tensile strength of the ground (see Table 1), a frost quake is assumed to occur and dissipate stress corresponding to 100% of the tensile strength. We keep a tally of the number of frost quakes over time and assume that multiple frost quakes occur if the tensile strength is exceeded by an integer factor greater than one. In reality, a fraction of the stress would be redistributed elastically rather than completely lost to friction as in this simple model. Since ground temperature is a measured quantity, we do not account for warming by frictional heat as a result of frost quake movement. Our aim is to model simple thermal tensional cracking of existing ice wedges or segregated ice bodies and not the initiation or propagation of new cracks into previously undamaged soil/bedrock, where pore scale fluid migration and stress localisation at crack tips become important (e.g. Walder and Hallet, 1985).

https://doi.org/10.5194/tc-2021-329
Preprint. Discussion started: 25 October 2021

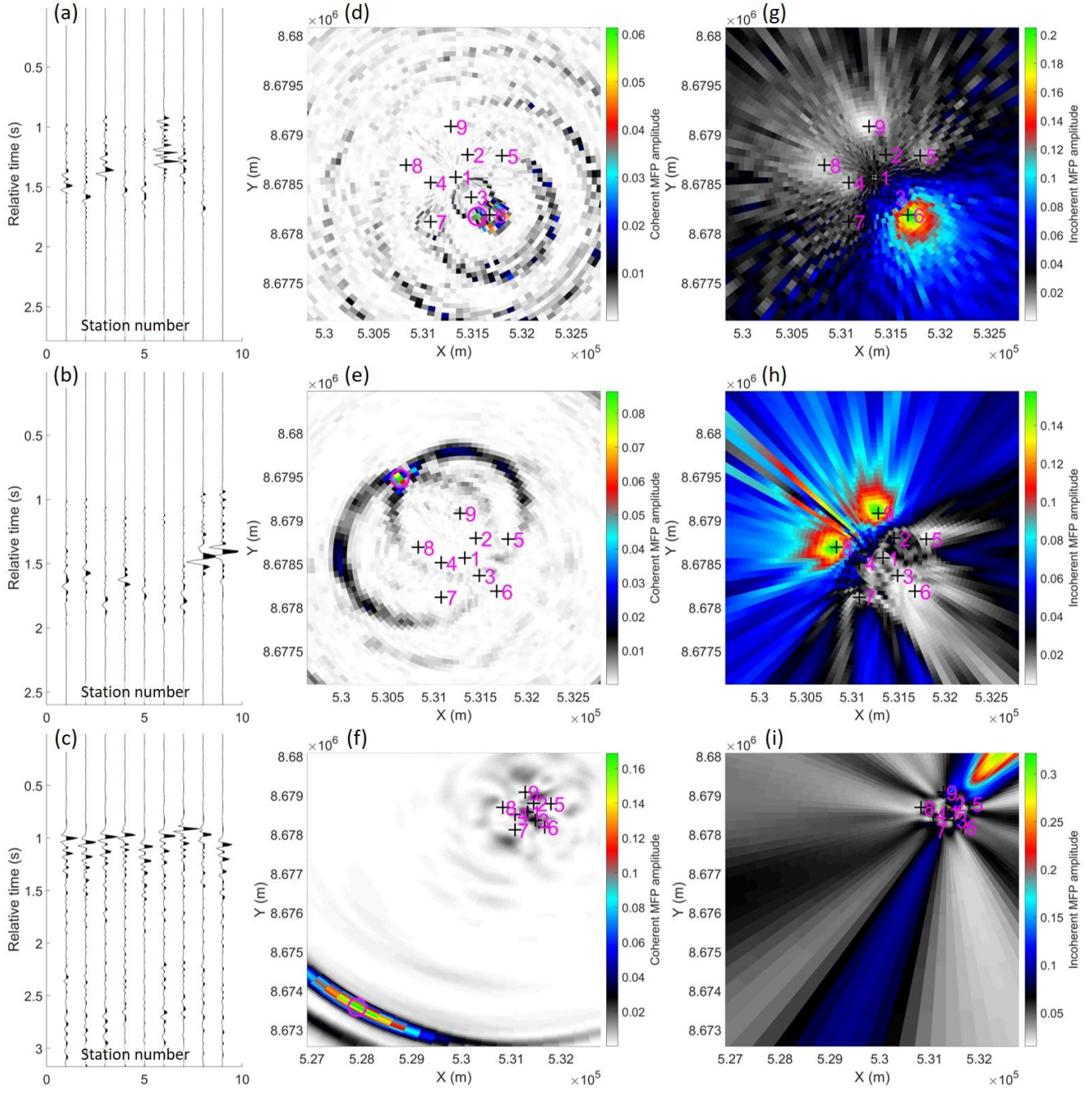

Figure 4 – (a), (b) Examples of Class I events with significant amplitude variation across the array and relatively close source position inferred by (d), (e) coherent MFP. (c) Example of a Class II event with little amplitude variation across the array and a more distal (f) coherent MFP inferred source position. (g), (h) & (i) show corresponding incoherent MFP results, Eq. (4), demonstrating the improvement gained by coherent MFP. Station numbers in (a), (b) & (c) correspond to the labels annotated on the MFP panels where the seismometer locations are marked with black crosses.

https://doi.org/10.5194/tc-2021-329
Preprint. Discussion started: 25 October 2021

4 Results and discussion

A total of 137,532 short duration seismic events were detected by our STA/LTA detector between July 2004 and June 2021. In order to improve the precision of the source localisation by coherent MFP, only events recorded by at least five seismometers were located for a total of 137,456 located short duration events. The estimated source locations were subsequently used to identify subclasses of events, as detailed in the following section.

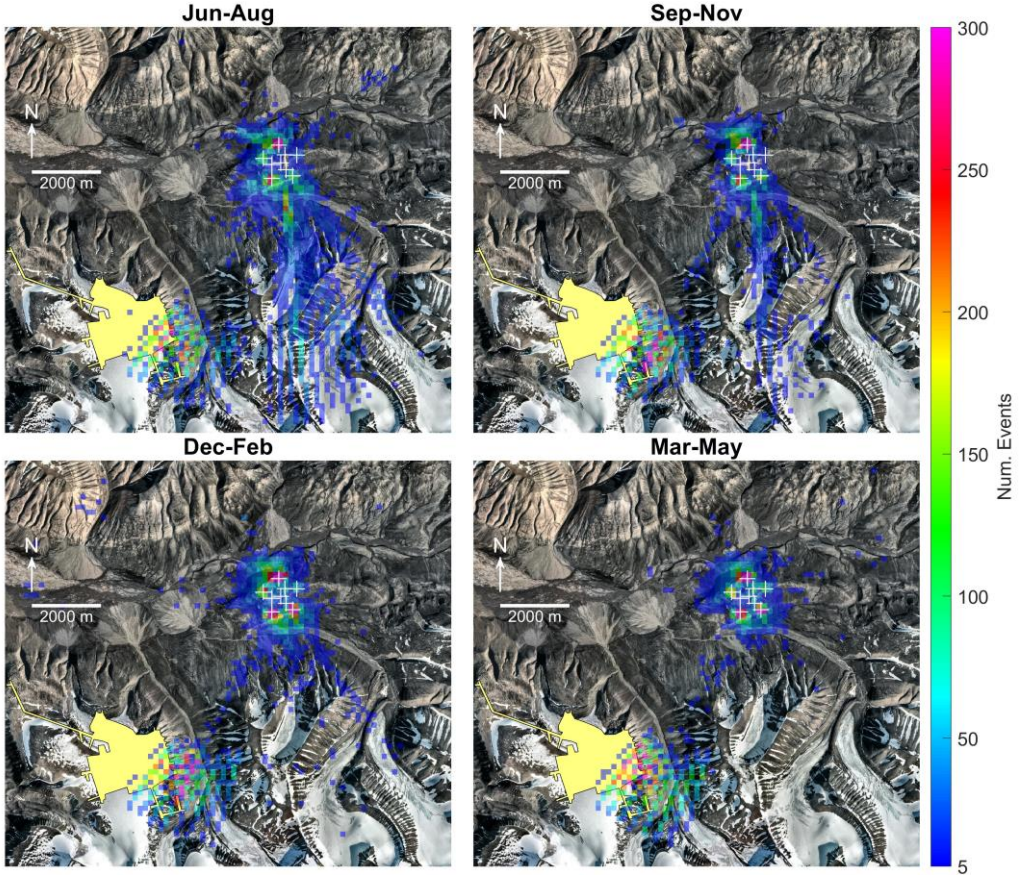

Figure 5 – Spatially binned (150×150 m) distribution of coherent MFP inferred seismic source positions plotted by season for events recorded between August 2004 and July 2021. Positions of SPITS seismometers are indicated by white crosses. The distal event cluster corresponds with the location of underground mining operations at Gruve 7 (yellow polygon). Orthophoto © Norwegian Polar Institute (npolar.no).

4.1 Subclasses of short duration seismic events

We find that there are two main sub-classes of short duration events recorded by the SPITS array. Event class I is characterised by significant amplitude variation and arrival time differences across the array seismometers, as illustrated in Figure 4a,b. Using coherent MFP to infer the source positions of these events, shows that they occur in relatively close proximity, within about 1500 m of the centroid of the array (Figure 4d,e). By contrast, Event class II is characterised by similar amplitudes across the array elements and smaller relative arrival time differences, as illustrated in (Figure 4c). Using coherent MFP, we find not

https://doi.org/10.5194/tc-2021-329
Preprint. Discussion started: 25 October 2021

only are these events associated with more distant sources (Figure 4f), they also have a consistent azimuth. Figure 4 also illustrates the property that coherent MFP decreases source localisation ambiguity for arrays that coarsely sample the spatial domain when compared to the incoherent scheme (Michalopoulou, 1998). In Figure 4i, we see that incoherent averaging (Eq. 4) has enhanced a sidelobe and produced an incorrect source position that is not consistent with the relative arrival times observed in Figure 4c.

The mean MFP inferred propagation velocities for Class I events was 1150 m/s with a standard deviation of 1100 m/s, indicating that they are dominated by surface waves. The large standard deviation may indicate the surface waves are dispersive with different frequencies propagating at different phase velocities. By contrast, the mean MFP inferred propagation velocity for Class II events was 5750 m/s with a standard deviation of 400 m/s, indicating that this event class is dominated by P-wave energy.

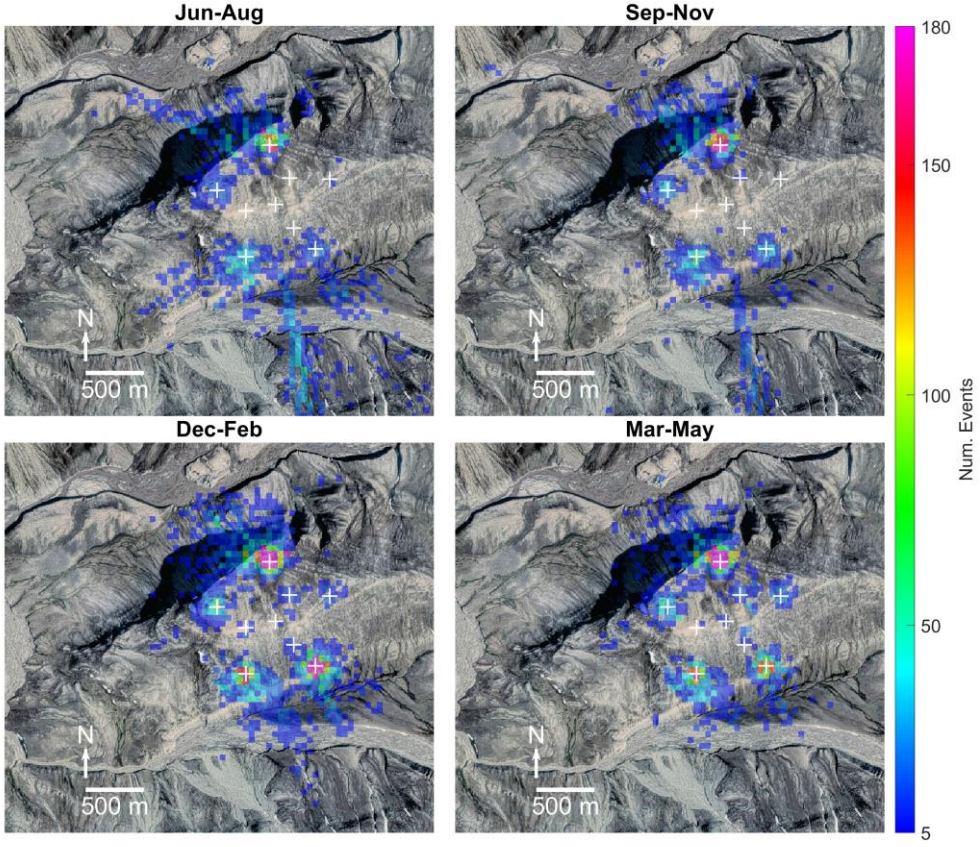

Figure 6 – Detail view of Janssonhaugen overlaid with spatially binned (50×50 m) distribution of coherent MFP inferred seismic source positions plotted by season for events recorded between August 2004 and July 2021. Positions of SPITS seismometers are indicated by white crosses. Orthophoto © Norwegian Polar Institute (npolar.no).

Mapping the inferred source positions, as in Figure 5, it is clear that Class II events are spatially coincident with the underground mining areas of Gruve 7. Furthermore, we observe that Class II events occur frequently during all seasons (see

https://doi.org/10.5194/tc-2021-329
Preprint. Discussion started: 25 October 2021

Figure 5). We infer that Event class II is a result of mining operations and human activity in the underground coal mine, Gruve 7. These events are essentially unwanted noise from the environmental seismology perspective, although they do give a useful indication of the localisation performance of the coherent MFP algorithm as applied in this study.

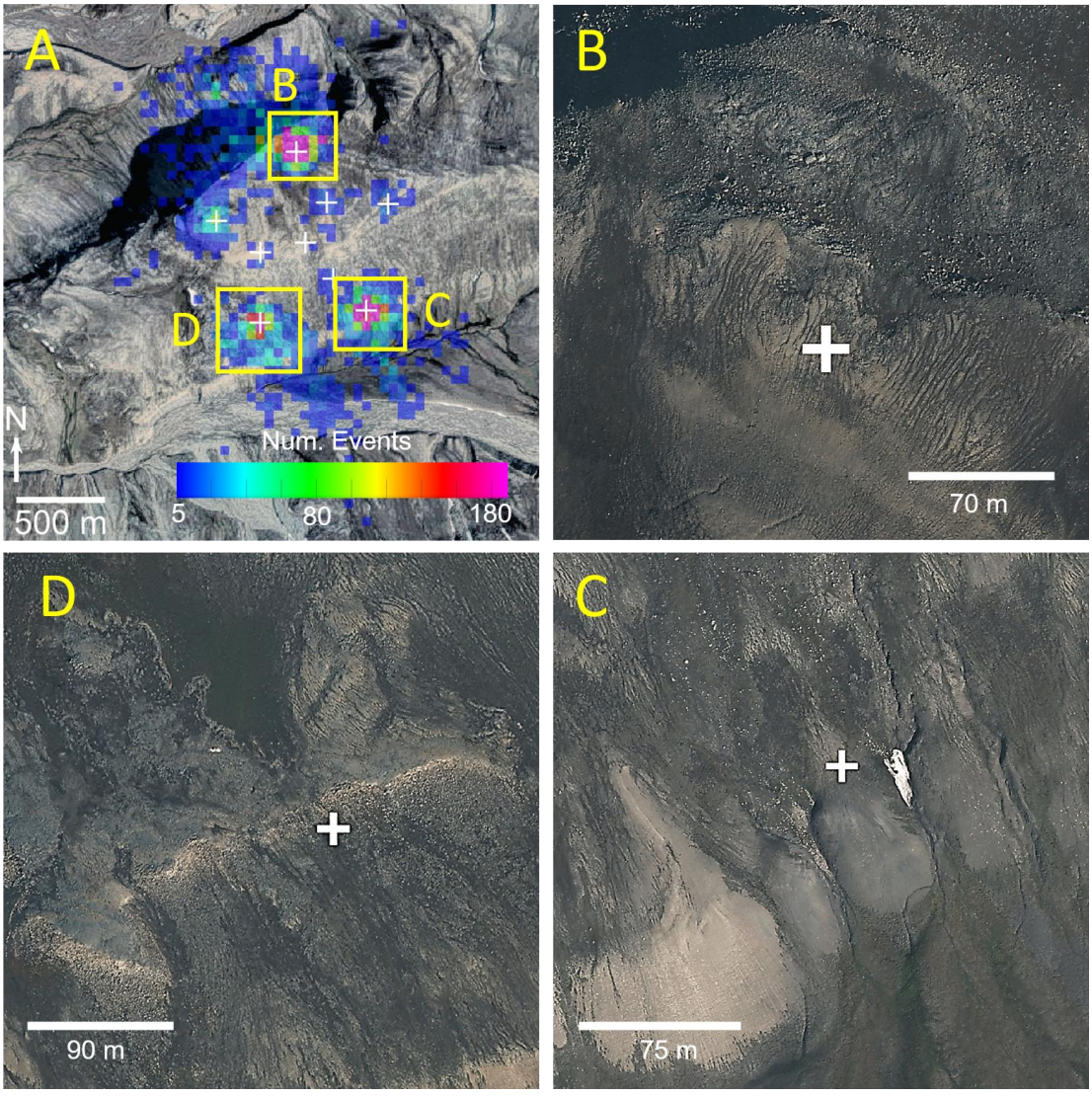

Figure 7 – (a) Dec-Feb events as plotted in Figure 6 with orthophotograph details illustrating the geomorphologic features associated with the most seismically active areas i.e. boulder producing scarps (b), (d) and solifluction lobes (b), (c). Orthophoto © Norwegian Polar Institute (npolar.no).

We observe a distinct seasonality for Class I events, with the highest detection rates occurring in the winter months (Dec-Feb) as illustrated in Figure 6. Detection rates are also high during the cold high-Arctic spring (Mar-May) and are lowest during the summer (Jun-August). We also observe a cluster of events due south of SPITS, with highest activity in the summer months, decreasing in the autumn (Sep-Nov) and absent during the winter and spring. These events may be rockfalls related to fluvial

https://doi.org/10.5194/tc-2021-329
Preprint. Discussion started: 25 October 2021

undercutting of steep river cliffs, rockfalls from steep mountain flanks or glacier/rock glacier movements. Using InSAR, Rouyet et al. (2019) measured high summer subsidence rates in the river valley, glacier/rock glacier and mountain flank areas south of Janssonhaugen corresponding to the inferred source locations of these seismic events. However, since the dynamics of these processes are not represented by our model, we were careful to exclude these events when spatially isolating Class I events. By selecting the subset of events with inferred source positions within ~1500 m of the array centroid and excluding the cluster of summer-autumn events due south of the array, we isolated a total of 42,432 class I events recorded between July 2004 and July 2021. Class I events occur most frequently during the cold winter and spring seasons, suggesting a relation to freezing processes.

Locally, the Class I seismicity is dominated by three source areas (see Figure 7) corresponding to areas with boulder producing scarps and solifluction lobes. These areas may be associated with enhanced ground heat loss, thin or absent snow cover or elevated ground moisture/ice content (e.g. Abolt et al., 2018; Matsuoka, 2008), though we lack the field observations necessary to support this explanation for the anomalous seismicity of these areas. The boulder producing scarps, particularly the one on the northern side of the array (Figure 6), in addition to the steep NW flank of Janssonhaugen, were also active during the summer thaw season. These thaw season events may be rockfalls due to melting of ice causing loss of strength or joint lubrication (Matsuoka, 2019; Weber et al., 2017).

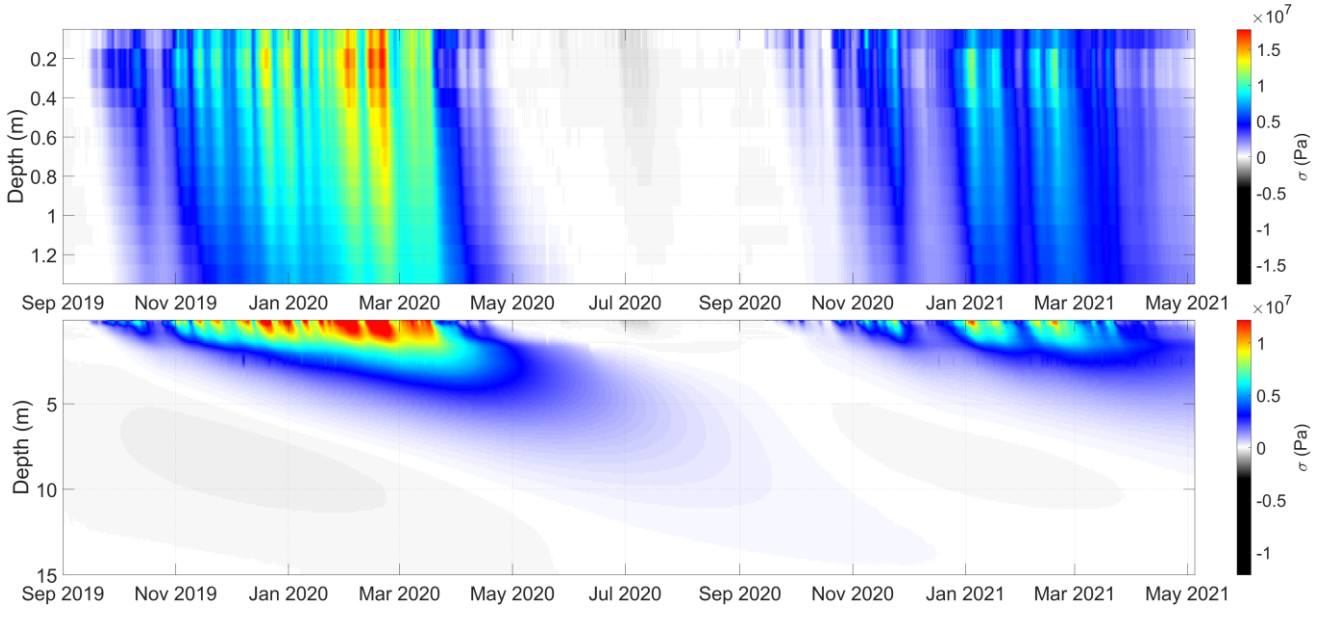

Figure 8 – Illustration of spatiotemporal thermal stress field modelled according to Eq. (12) and constrained by temperature measurements recorded by sensors installed at Janssonhaugen Vest (0.1 m) and in the P11 borehole (0.2-15 m).

https://doi.org/10.5194/tc-2021-329
Preprint. Discussion started: 25 October 2021

340 **4.2 Modelled thermal stress**

Figure 8 illustrates the spatiotemporal thermal stress field that was modelled by solving Eq. (12) using the parameters listed in Table 1 and a combination of the 0.1 m ground temperature timeseries recorded at the Janssonhaugen Vest meteorological station and the 0.2-15 m temperatures recorded in the P11 borehole. The largest thermal stresses occur in the active layer, which is subject to large amplitude winter cooling cycles. Since the peak annual stresses occur at 0.2 m depth and we have a 345 much longer record from the P11 borehole compared to the Janssonhaugen Vest meteorological station, we focus on this horizon as the dominant frost cracking depth throughout the rest of the study. That peak thermal stress is modelled at 0.2 m is interesting as it corresponds with the 20-30cm thick regolith layer at Janssonhaugen (Isaksen et al., 2001), suggesting that in-situ frost cracking may have weathered the bedrock to produce the surficial layer. Frost polygons in this region are interpreted to be very old (Sørbel and Tolgensbakk, 2002) so there has likely been sufficient time to reach a steady state condition. If frost 350 cracking extended much deeper, we would expect that repeated cracking over thousands of years would have produced a thicker regolith layer than that which is observed.

4.3 Thermal stress associated with seismic events

Figure 9 illustrates the shallowest measured temperature profiles and corresponding thermal stress for the Sep 2019 to Jun 2021 period. The Class II events, corresponding to mining activities at Gruve 7, have source ranges of 6000-7000 m with a 355 consistent azimuth of ~210° and no correspondence with thermal stress. On the other hand, Class I events have variable azimuths but source ranges <1500 m and tend to be associated with peaks in thermal stress.

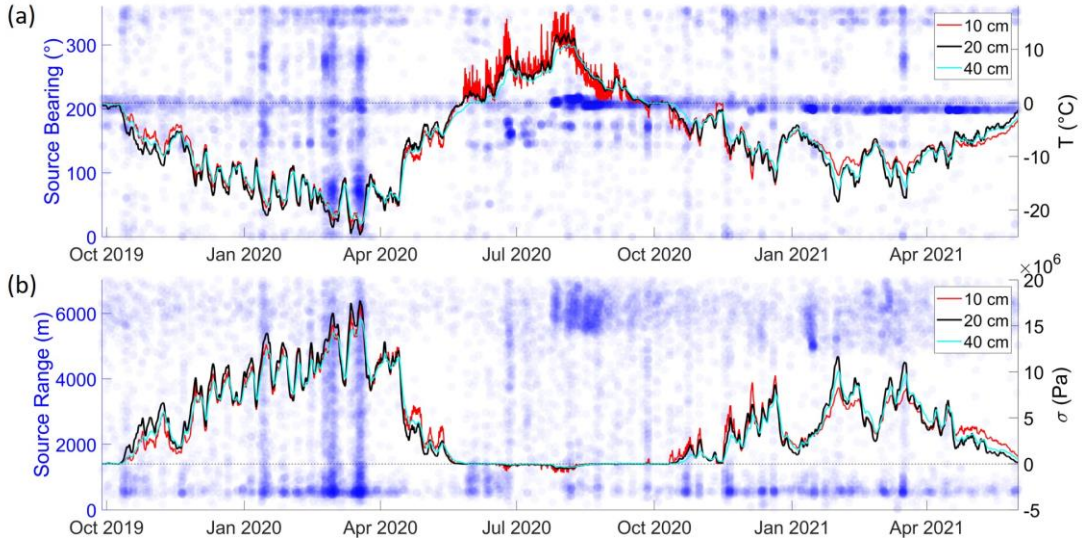

Figure 9 – (a) Ground temperature profiles (solid lines) and bearing (clockwise from North) to coherent MFP localised source 360 **positions from centre of SPITS array (blue circles). (b) modelled ground thermal stress from Eq. (12) (solid lines) and ranges to**

https://doi.org/10.5194/tc-2021-329
Preprint. Discussion started: 25 October 2021

coherent MFP localised sources (blue circles). Source ranges and azimuths are transparent such that denser colours represent clusters of events.

Figure 10 shows a detailed comparison of the Class I seismicity and the modelled frequency of tensile fracturing due to thermal stresses exceeding the assumed tensile strength of the medium (as described in Section 3.3.1). Given that seismicity is a complex, stochastic process in time and space, our simple thermal stress-based fracture model does a reasonably good job of capturing the time periods and approximate frequency of the Class I events. This leads us to infer that thermal contraction cracking of segregated ice bodies, as modelled by Eq. (12) is a significant process contributing to event Class I seismicity. The clusters of events recorded June-August, when thermal stress is low (see Figure 6 and Figure 10), are most likely rockfalls on the steep boulder producing scarps (see Figure 7) initiated by melting of fracture-filling ice leading to loss of strength or joint lubrication (Matsuoka, 2019; Weber et al., 2017).

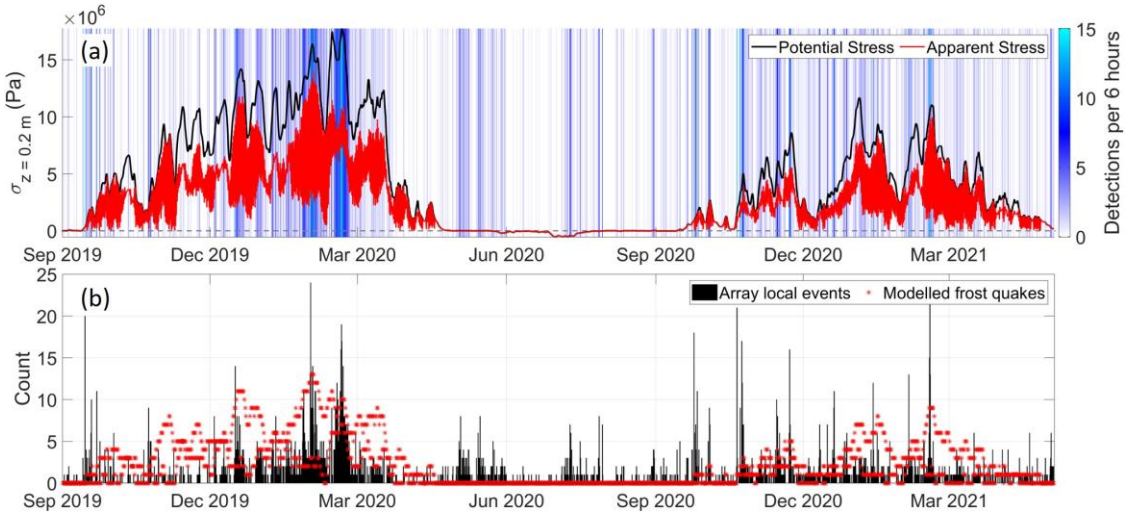

Figure 10 – (a) Potential thermal stress (black) given by the solution to Eq. (12) and apparent thermal stress accounting for stress release by frost cracking (red) with blue colour gradient indicating the detection rate of Class I events. (b) modelled number of frost quakes (red) and frequency histogram of Class I events (black).

A similar association between Class I events and peaks in thermal stress persists over the entire study period, from 2004-2021 (see Figure 11). Figure 12 shows that the modelled and observed frost quake seismicity also matches quite well over the study period (the normalised cross correlation is 0.61), though the observed seismicity has a tendency to occur in more defined periods than predicted by the model, resulting in a relatively spiky frequency histogram. Examples of anomalous seismicity not explained by the model are the periods 17-26 Feb 2010, 7-16 Feb, 2012 and 8-17 Jan 2016 (see Figure 12). While these periods of enhanced seismicity are still associated with peaks in thermal stress, our simple model is unable to explain the intensity of seismicity in these periods relative to, e.g., earlier periods in the same seasons with similar thermal stress but fewer Class I events (see Figure 11). There are likely multiple factors for this deviation, including the inherently stochastic nature of seismicity. However, there are likely also systematic factors that are simply not accounted for in our model like the spatial redistribution of stress between multiple fractures and across multiple depths. In addition, the mild temperatures preceding

https://doi.org/10.5194/tc-2021-329
Preprint. Discussion started: 25 October 2021

these episodes of enhanced seismicity (seen as pronounced drops in stress in Figure 11) may have produced unfrozen water and conditions favourable for the formation of new ice lenses (Hallet et al., 1991; Murton et al., 2006; Peppin and Style, 2013; Walder and Hallet, 1985). That is, there are other processes that can drive frost cracking in addition to the thermal contraction cracking of segregated ice bodies and ice wedges that is favoured by our model. We speculate that the inability of the thermal contraction model to explain the anomalously high levels of seismicity in the periods 17-26 Feb 2010, 7-16 Feb, 2012 and 8-17 Jan 2016 provides evidence that capillary and frozen-fringe effects are also important (Peppin and Style, 2013).

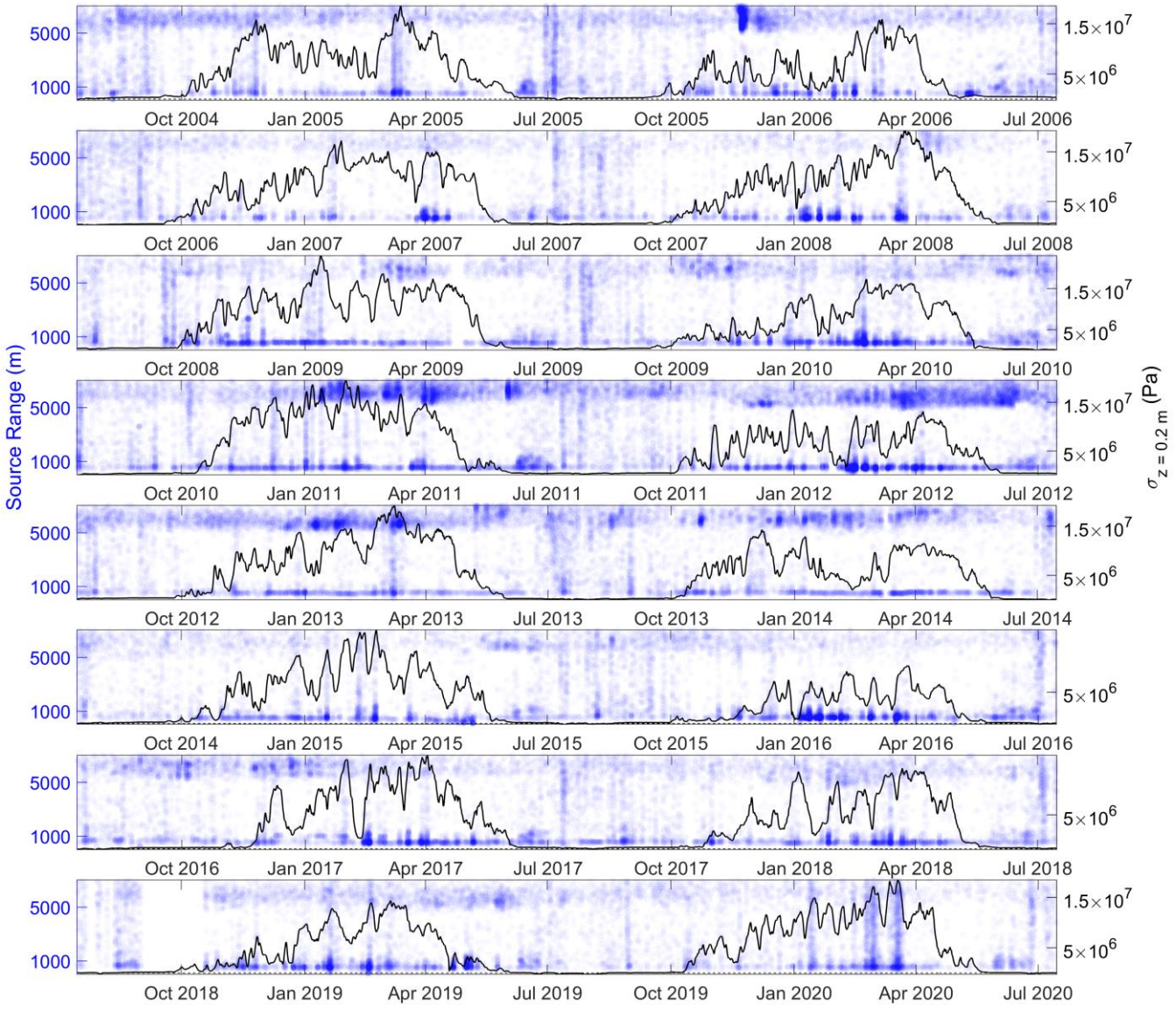

Figure 11 – Modelled thermal stress from Eq. (12) at 0.2 m depth (black lines) and ranges to coherent MFP localised sources (blue circles). Source ranges and azimuths are plotted as transparent points such that denser colours represent clusters of events. Event class I & II are associated with small (<1500 m) and large (>5000 m) source ranges, respectively.

https://doi.org/10.5194/tc-2021-329
Preprint. Discussion started: 25 October 2021

We consider the use of real ground temperature measurements a strength of this study, since the subsurface temperature field is a complex product of sensible, latent and convective heat fluxes, depending on matrix and pore-filling material properties as well as surface properties like the thermal conductivity of snow (e.g. Badache et al., 2016; Rankinen et al., 2004). However, it is important to recognize that the P11 borehole and Janssonhaugen Vest ground temperature measurements are point samples of a temperature field that may vary spatially according to local geomorphology and variation in snow cover. For example, Abolt et al. (2018) have demonstrated that ground under the elevated rims of frost polygons cools significantly faster than the depressed centres due to decreased snow cover. Accounting for variation on the local scale fell outside the scope of the present study, but extending the model framework to allow stochastic temperature variation via stochastic differential equations may give additional insight into the significance of local scale variability.

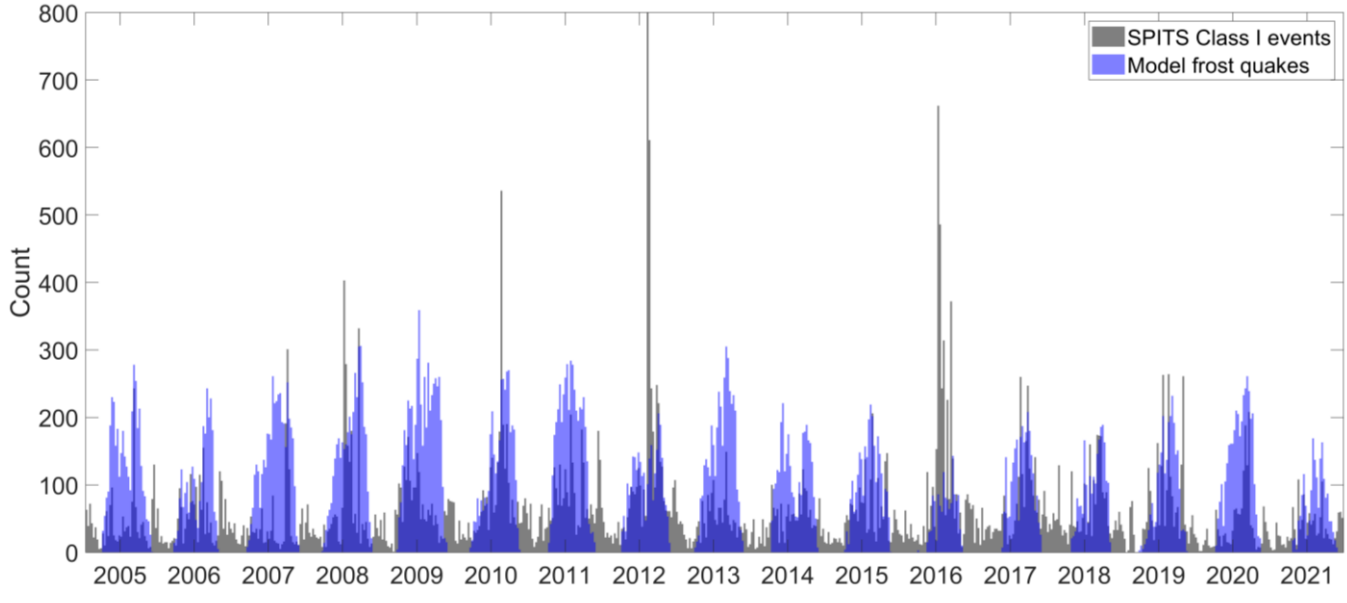

Figure 12 – Histogram binned to 9-day intervals comparing the modelled frost quake frequency (blue) with the recorded frequency of Class I events (black).

5 Conclusion

We studied the spatial and temporal patterns of the class of seismicity that lead to short duration ground shaking at the SPITS array in Adventdalen, based on a catalogue of >100 000 events recorded between 2004 and 2021. To the best of our knowledge, this is a uniquely large and long spanning event catalogue amongst studies with a focus on cryoseisms. We find that these short duration seismic events, with ground motion lasting just a few seconds, can be grouped into two main subclasses. One class is clearly associated with mining activities at the underground coal mine, Gruve 7 and is mostly useful as an indicator of the performance of the coherent-MFP source localisation algorithm. The other subclass of short duration seismic events is interpreted to be dominated by frost quakes produced by thermal contraction cracking of ice wedges or other sub-surface

https://doi.org/10.5194/tc-2021-329
Preprint. Discussion started: 25 October 2021

segregated ice bodies. These events appear to be dominated by surface wave energy and source positions that are proximal to the SPITS array, particularly three areas that are associated with dynamic geomorphological features; boulder producing scarps and solifluction lobes. Temporally these events are associated with peaks in ground thermal stress as modelled by a simple dynamical thermo-viscoelastic model constrained by borehole measurements of ground temperature. The long term continuous observational record, containing tens of thousands of inferred cryoseismic events, in proximity to high-quality borehole temperature observations, provides a unique insight into the spatiotemporal patterns of cryoseismicity.

6 Acknowledgments

This research is funded by the University of Tromsø - The Arctic University of Norway, by the ARCEx partners and by the Research Council of Norway through grant number 228107. The publication charges for this article have been funded by a grant from the publication fund of UiT The Arctic University of Norway.

7 References

Abolt, C. J., Young, M. H., Atchley, A. L., and Harp, D. R.: Microtopographic control on the ground thermal regime in ice wedge polygons, The Cryosphere, 12, 1957-1968, 2018.

Albaric, J., Kühn, D., Ohrnberger, M., Langet, N., Harris, D., Polom, U., Lecomte, I., and Hillers, G.: Seismic monitoring of permafrost in Svalbard, Arctic Norway, Seismological Society of America, 92, 2891-2904, 2021.

Badache, M., Eslami-Nejad, P., Ouzzane, M., Aidoun, Z., and Lamarche, L.: A new modeling approach for improved ground temperature profile determination, Renewable Energy, 85, 436-444, 2016.

Barosh, P. J.: Frostquakes in New England, Engineering Geology, 56, 389-394, 2000.

Battaglia, S. M., Changnon, D., Changnon, D., and Hall, D.: Frost quake events and changing wintertime air mass frequencies in southeastern Canada, Working Paper, Northern Illinois University. doi: 10.13140/RG. 2.2. 22351.48803, 2016.

Behn, M. D., Goldsby, D. L., and Hirth, G.: The role of grain size evolution in the rheology of ice: implications for reconciling laboratory creep data and the Glen flow law, The Cryosphere, 15, 4589-4605, 2021.

Bingham, E. C.: Fluidity and plasticity, McGraw-Hill, 1922.

Black, R. F.: Periglacial features indicative of permafrost: ice and soil wedges, Quaternary Research, 6, 3-26, 1976.

Butkovich, T.: Thermal expansion of ice, Journal of Applied Physics, 30, 350-353, 1959.

Cable, S., Elberling, B., and Kroon, A.: Holocene permafrost history and cryostratigraphy in the High-Arctic Adventdalen Valley, central Svalbard, Boreas, 47, 423-442, 2018.

Carreau, P. J.: Rheological equations from molecular network theories, Transactions of the Society of Rheology, 16, 99-127, 1972.

Chen, J., Wu, Y., O'Connor, M., Cardenas, M. B., Schaefer, K., Michaelides, R., and Kling, G.: Active layer freeze-thaw and water storage dynamics in permafrost environments inferred from InSAR, Remote Sensing of Environment, 248, 112007, 2020.

Chmiel, M., Roux, P., and Bardainne, T.: Extraction of phase and group velocities from ambient surface noise in a patch-array configuration, Geophysics, 81, KS231-KS240, 2016.

Christiansen, H. H., Gilbert, G., Demidov, N., Guglielmin, M., Isaksen, K., Osuch, M., and Boike, J.: Permafrost temperatures and active layer thickness in Svalbard during 2017/2018 (PermaSval), SESS Report 2019-The State of Environmental Science in Svalbard, 2020. 2020.

Christiansen, H. H., Matsuoka, N., and Watanabe, T.: Progress in understanding the dynamics, internal structure and palaeoenvironmental potential of ice wedges and sand wedges, Permafrost and Periglacial Processes, 27, 365-376, 2016.

Cros, E., Roux, P., Vandemeulebrouck, J., and Kedar, S.: Locating hydrothermal acoustic sources at Old Faithful Geyser using matched field processing, Geophysical Journal International, 187, 385-393, 2011.

Currier, J. and Schulson, E.: The tensile strength of ice as a function of grain size, Acta Metallurgica, 30, 1511-1514, 1982.

DiMillio, A. F.: A quarter century of geotechnical research, Turner-Fairbank Highway Research Center, 1999.

Dormand, J. R. and Prince, P. J.: A family of embedded Runge-Kutta formulae, Journal of computational and applied mathematics, 6, 19-26, 1980.

Draebing, D. and Krautblatter, M.: P-wave velocity changes in freezing hard low-porosity rocks: a laboratory-based time-average model, The Cryosphere, 6, 1163-1174, 2012.

Dypvik, H., Nagy, J., Eikeland, T., Backer-Owe, K., and Johansen, H.: Depositional conditions of the Bathonian to Hauterivian Janusfjellet subgroup, Spitsbergen, Sedimentary Geology, 72, 55-78, 1991.

French, H. M.: The periglacial environment, John Wiley & Sons, 2017.

Gibbons, S. J. and Ringdal, F.: The detection of low magnitude seismic events using array-based waveform correlation, Geophysical Journal International, 165, 149-166, 2006.

Gibbons, S. J., Schweitzer, J., Ringdal, F., Kværna, T., Mykkeltveit, S., and Paulsen, B.: Improvements to seismic monitoring of the European Arctic using three-component array processing at SPITS, Bulletin of the Seismological Society of America, 101, 2737-2754, 2011.

Glen, J. W.: The creep of polycrystalline ice, Proceedings of the Royal Society of London. Series A. Mathematical and Physical Sciences, 228, 519-538, 1955.

Hales, T. and Roering, J.: A frost “buzzsaw” mechanism for erosion of the eastern Southern Alps, New Zealand, Geomorphology, 107, 241-253, 2009.

Hales, T. and Roering, J. J.: Climatic controls on frost cracking and implications for the evolution of bedrock landscapes, Journal of Geophysical Research: Earth Surface, 112, 2007.

Hallet, B., Walder, J., and Stubbs, C.: Weathering by segregation ice growth in microcracks at sustained subzero temperatures: Verification from an experimental study using acoustic emissions, Permafrost and Periglacial Processes, 2, 283-300, 1991.

Hanssen, R. F.: Radar interferometry: data interpretation and error analysis, Springer Science & Business Media, 2001.

Harley, J. B. and Moura, J. M.: Data-driven matched field processing for Lamb wave structural health monitoring, The Journal of the Acoustical Society of America, 135, 1231-1244, 2014.

Herschel, W.: Measurement of consistency of rubber-benzene solutions, Kolloid-zeitschrift, 39, 291-298, 1926.

Hu, X.-d., Wang, J.-t., and Yu, R.-z.: Uniaxial compressive and splitting tensile tests of artificially frozen soils in tunnel construction of Hong Kong, Journal of Shanghai Jiaotong University (Science), 18, 688-692, 2013.

Isaksen, K., Holmlund, P., Sollid, J. L., and Harris, C.: Three deep alpine-permafrost boreholes in Svalbard and Scandinavia, Permafrost and Periglacial Processes, 12, 13-25, 2001.

Isaksen, K., Mühll, D. V., Gubler, H., Kohl, T., and Sollid, J. L.: Ground surface-temperature reconstruction based on data from a deep borehole in permafrost at Janssonhaugen, Svalbard, Ann Glaciol, 31, 287-294, 2000.

Istomin, A. and Nazarov, T.: Numerical studies of reinforced concrete pile foundations on permafrost soils at low climatic temperatures, 2019, 012082.

Kell, G.: Precise representation of volume properties of water at one atmosphere, Journal of Chemical and Engineering data, 12, 66-69, 1967.

Köhler, A., Nuth, C., Schweitzer, J., Weidle, C., and Gibbons, S. J.: Regional passive seismic monitoring reveals dynamic glacier activity on Spitsbergen, Svalbard, Polar Research, 34, 26178, 2015.

Lachenbruch, A. H.: Mechanics of thermal contraction cracks and ice-wedge polygons in permafrost, Geological Society of America, 1962.

Lacroix, A. V.: A short note on cryoseisms, Earthquake Notes, 51, 15-21, 1980.

Landau, L. and Lifshitz, E.: Theory of Elasticity, 2nd Edition. Pergamon Press, Oxford, 1970.

Leung, A. C., Gough, W. A., and Shi, Y.: Identifying frostquakes in Central Canada and neighbouring regions in the United States with social media. In: Citizen Empowered Mapping, Springer, 2017.

Liu, L., Rouyet, L., Strozzi, T., Lauknes, T. R., and Christiansen, H. H.: Seasonal Thaw Settlement and Frost Heave in Permafrost Regions in the Arctic: A Synthesis of InSAR Observations Using Sentinel-1 SAR Images, 2018, GC31B-05.

Mackay, J. R.: The direction of ice-wedge cracking in permafrost: downward or upward?, Canadian Journal of Earth Sciences, 21, 516-524, 1984.

Maloof, A. C., Kellogg, J. B., and Anders, A. M.: Neoproterozoic sand wedges: crack formation in frozen soils under diurnal forcing during a snowball Earth, Earth and Planetary Science Letters, 204, 1-15, 2002.

Matsuoka, N.: Frost weathering and rockwall erosion in the southeastern Swiss Alps: Long-term (1994–2006) observations, Geomorphology, 99, 353-368, 2008.

Matsuoka, N.: A multi-method monitoring of timing, magnitude and origin of rockfall activity in the Japanese Alps, Geomorphology, 336, 65-76, 2019.

Matsuoka, N.: Solifluction rates, processes and landforms: a global review, Earth-Science Reviews, 55, 107-134, 2001.

https://doi.org/10.5194/tc-2021-329
Preprint. Discussion started: 25 October 2021

Matsuoka, N., Christiansen, H. H., and Watanabe, T.: Ice-wedge polygon dynamics in Svalbard: Lessons from a decade of automated multi-sensor monitoring, Permafrost and Periglacial Processes, 29, 210-227, 2018.

Matsuoka, N., Sawaguchi, S.-i., and Yoshikawa, K.: Present-day periglacial environments in central Spitsbergen, Svalbard, Geographical Review of Japan, 77, 276-300, 2004.

Mellon, M. T.: Small-scale polygonal features on Mars: Seasonal thermal contraction cracks in permafrost, Journal of Geophysical Research: Planets, 102, 25617-25628, 1997.

Michalopoulou, Z. H.: Robust multi-tonal matched-field inversion: A coherent approach, The Journal of the Acoustical Society of America, 104, 163-170, 1998.

Murton, J. B., Peterson, R., and Ozouf, J.-C.: Bedrock fracture by ice segregation in cold regions, Science, 314, 1127-1129, 2006.

Nikonov, A.: Frost quakes as a particular class of seismic events: Observations within the East-European platform, Izvestiya, Physics of the Solid Earth, 46, 257-273, 2010.

Okkonen, J., Neupauer, R., Kozlovskaya, E., Afonin, N., Moisio, K., Taewook, K., and Muurinen, E.: Frost Quakes: Crack Formation by Thermal Stress, Journal of Geophysical Research: Earth Surface, 125, e2020JF005616, 2020.

Peppin, S. S. and Style, R. W.: The physics of frost heave and ice-lens growth, Vadose Zone Journal, 12, 2013.

Podolskiy, E. A., Fujita, K., Sunako, S., and Sato, Y.: Viscoelastic Modeling of Nocturnal Thermal Fracturing in a Himalayan Debris-Covered Glacier, Journal of Geophysical Research: Earth Surface, 124, 1485-1515, 2019.

Rabiner, L. R., Schafer, R. W., and Rader, C. M.: The chirp z-transform algorithm and its application, Bell System Technical Journal, 48, 1249-1292, 1969.

Rankinen, K., Karvonen, T., and Butterfield, D.: A simple model for predicting soil temperature in snow-covered and seasonally frozen soil: model description and testing, Hydrology and Earth System Sciences, 8, 706-716, 2004.

Rempel, A. W.: Frost heave, Journal of Glaciology, 56, 1122-1128, 2010.

Romeyn, R., Hanssen, A., Ruud, B. O., Stemland, H. M., and Johansen, T. A.: Passive seismic recording of cryoseisms in Adventdalen, Svalbard, The Cryosphere, 15, 283-302, 2021.

Rosen, P. A., Hensley, S., Joughin, I. R., Li, F. K., Madsen, S. N., Rodriguez, E., and Goldstein, R. M.: Synthetic aperture radar interferometry, Proceedings of the IEEE, 88, 333-382, 2000.

Rouyet, L., Lauknes, T. R., Christiansen, H. H., Strand, S. M., and Larsen, Y.: Seasonal dynamics of a permafrost landscape, Adventdalen, Svalbard, investigated by InSAR, Remote Sensing of Environment, 231, 111236, 2019.

Rouyet, L., Liu, L., Strand, S. M., Christiansen, H. H., Lauknes, T. R., and Larsen, Y.: Seasonal InSAR Displacements Documenting the Active Layer Freeze and Thaw Progression in Central-Western Spitsbergen, Svalbard, Remote Sensing, 13, 2977, 2021.

Saramito, P.: A new constitutive equation for elastoviscoplastic fluid flows, Journal of Non-Newtonian Fluid Mechanics, 145, 1-14, 2007.

Scherler, D.: Climatic limits to headwall retreat in the Khumbu Himalaya, eastern Nepal, Geology, 42, 1019-1022, 2014.

https://doi.org/10.5194/tc-2021-329
Preprint. Discussion started: 25 October 2021

Schulson, E. M. and Duval, P.: Creep and fracture of ice, Cambridge university press, 2009.

Schweitzer, J., Köhler, A., and Christensen, J. M.: Development of the NORSAR Network over the Last 50 Yr, Seismological Society of America, 92, 1501-1511, 2021.

Sergeant, A., Chmiel, M., Lindner, F., Walter, F., Roux, P., Chaput, J., Gimbert, F., and Mordret, A.: On the Green's function emergence from interferometry of seismic wave fields generated in high-melt glaciers: implications for passive imaging and monitoring, The Cryosphere, 14, 1139-1171, 2020.

Sørbel, L. and Tolgensbakk, J.: Ice-wedge polygons and solifluction in the Adventdalen area, Spitsbergen, Svalbard, Norsk Geografisk Tidsskrift-Norwegian Journal of Geography, 56, 62-66, 2002.

Timoshenko, S. and Goodier, J.: Theory of Elasticity, McGraw-Hill book Company, New York, 1951.

Timur, A.: Velocity of compressional waves in porous media at permafrost temperatures, Geophysics, 33, 584-595, 1968.

Trnkoczy, A.: Understanding and parameter setting of STA/LTA trigger algorithm. In: New Manual of Seismological Observatory Practice (NMSOP), Deutsches GeoForschungsZentrum GFZ, 2009.

Wahr, J., Liu, L., and Zhang, T.: InSAR measurements of ground surface deformation due to thaw settlement and frost heave over permafrost on the North Slope of Alaska, 2008, C13B-02.

Walder, J. and Hallet, B.: A theoretical model of the fracture of rock during freezing, Geological Society of America Bulletin, 96, 336-346, 1985.

Walter, F., Roux, P., Roeoesli, C., Lecointre, A., Kilb, D., and Roux, P.-F.: Using glacier seismicity for phase velocity measurements and Green's function retrieval, Geophysical Journal International, 201, 1722-1737, 2015.

Weber, S., Beutel, J., Faillettaz, J., Hasler, A., Krautblatter, M., and Vieli, A.: Quantifying irreversible movement in steep, fractured bedrock permafrost on Matterhorn (CH), The Cryosphere, 11, 567-583, 2017.

Weeks, W. F. and Assur, A.: The Mechanical Properties of Sea Ice, Cold Regions Research & Engineering Laboratory, Hanover, New Hampshire, 1967.

Weertman, J.: Creep deformation of ice, Annual Review of Earth and Planetary Sciences, 11, 215-240, 1983.

Wu, Y., Nakagawa, S., Kneafsey, T. J., Dafflon, B., and Hubbard, S.: Electrical and seismic response of saline permafrost soil during freeze-thaw transition, J Appl Geophys, 146, 16-26, 2017.

Zhankui, Y., Yuanling, Z., and Ping, H.: Experimental study of Poisson's ratio for frozen soil, 1998, 1185-1186.

8 Code/Data availability

All data used in this study is publicly available, seismic waveform data may be downloaded via http://eida.geo.uib.no. The Janssonhaugen P11 temperature monitoring borehole is part of the GTN-P database (Global Terrestrial Network for Permafrost) and data is available upon request to the custodian. Meteorological data (including ground temperature) from the

https://doi.org/10.5194/tc-2021-329
Preprint. Discussion started: 25 October 2021

Janssonhaugen Vest weather station is available via the Norwegian Centre for Climate Services https://seklima.met.no/. The code used to produce this research can be shared upon request to the authors.

9 Author contribution

The study was conceptualised by AK and RR. The model, theory and methodology were developed by RR and AH. RR carried out the data collation and processing and was responsible for analysing and visualising the data. RR drafted the initial manuscript with contributions from all authors, with AH contributing significantly to the development and drafting of the theory sections. AH and AK also provided project supervision.

10 Competing interests

The authors of this article declare that they have no conflict of interest.